minerals

MDPI

Article

Tourmaline Composition of the Kışladağ Porphyry Au Deposit, Western Turkey: Implication of Epithermal Overprint

Ömer Bozkaya [1,*], Ivan A. Baksheev [2], Nurullah Hanilçi [3], Gülcan Bozkaya [1], Vsevolod Y. Prokofiev [4], Yücel Öztaş [5] and David A. Banks [6]

1 Department of Geological Engineering, Pamukkale University, 20070 Denizli, Turkey; gbozkaya@pau.edu.tr
2 Department of Geology, Moscow State University, Leninskie Gory, 119991 Moscow, Russia; baksheev@geol.msu.ru
3 Department of Geological Engineering, Istanbul University-Cerrahpaşa, Avcılar, 34320 Istanbul, Turkey; nurullah@istanbul.edu.tr
4 Institute of Geology of Ore Deposits, Petrography, Mineralogy and Geochemistry, Russian Academy of Sciences, 119017 Moscow, Russia; vpr2004@rambler.ru
5 TÜPRAG Metal Madencilik, Ovacık Mevki Gümüşkol Köyü, Ulubey Merkez, 64902 Uşak, Turkey; yucelo@kisladag.com
6 School of Earth and Environment, University of Leeds, Leeds LS2 9JT, UK; D.A.Banks@leeds.ac.uk
* Correspondence: obozkaya@pau.edu.tr; Tel.: +90-258-296-3442

Received: 13 August 2020; Accepted: 4 September 2020; Published: 7 September 2020

Abstract: The Kışladağ porphyry Au deposit occurs in a middle Miocene magmatic complex comprising three different intrusions and magmatic-hydrothermal brecciation related to the multiphase effects of the different intrusions. Tourmaline occurrences are common throughout the deposit, mostly as an outer alteration rim around the veins with lesser amounts disseminated in the intrusions, and are associated with every phase of mineralization. Tourmaline mineralization has developed as a tourmaline-rich matrix in brecciated zones and tourmaline-quartz and/or tourmaline-sulfide veinlets within the different intrusive rocks. Tourmaline was identified in the tourmaline-bearing breccia zone (TBZ) and intrusive rocks that had undergone potassic, phyllic, and advanced argillic alteration. The tourmaline is present as two morphological varieties, aggregates of fine crystals (rosettes, fan-shaped) and larger isolated crystals and their aggregates. Four tourmaline generations (tourmaline I to IV) have different compositions and substitutions. Tourmaline I in TBZ and INT#1 is distinguished by the highest Fe_{tot} and enriched in Fe^{3+}. Tourmalines II and III occur as fine aggregates, accompanied by the formation of isolated crystals and are characterized by lower Fe_{tot} and Fe^{3+}. Tourmaline IV is characterized by the lowest Fe_{tot}, enriched in Cl, and has the highest proportion of X-site vacancy among all the tourmalines. Tourmaline I may be attributed to the potassic stage in INT#1 and early tourmaline in TBZ. Tourmalines II and III from INT#1 and the TBZ could be referred to the phyllic stage. The low Fe content in tourmaline is caused by the simultaneous deposition of sulfide minerals. Tourmaline IV from the TBZ and tourmaline II from INT#3 are distinguished by the high X-site vacancy proportion up to the formation of X-site vacant species as well as enriched in Cl; they can be attributed to the argillic stage of the hydrothermal process. The textural and especially chemical data of the tourmaline from the Kışladağ Au deposit provide information on the physico-chemical conditions during the porphyry to epithermal transition and subsequent epithermal overprinting.

Keywords: tourmaline; mineral chemistry; porphyry Au deposit; Kışladağ; Turkey

1. Introduction

Tourmaline is a complex borosilicate mineral group that has a general structural formula of $XY_3Z_6[T_6O_{18}](BO_3)_3V_3W$, where X = Na, Ca, K, and vacancy (□), Y = Li^+, Mg^{2+}, Fe^{2+}, Mn^{2+}, Al^{3+}, and Ti^{4+}, Z = Al^{3+}, Mg^{2+}, Fe^{3+}, V^{3+}, and Cr^{3+}, T = Si, Al, and B, V = OH, O, and W = OH, O, and F [1–3]. It occurs in a variety of geological environments and is a common accessory mineral in granitic pegmatites, low- to high-grade metamorphic rocks, and clastic sedimentary rocks. However, it is in the porphyry-hydrothermal environments where diverse occurrences such as gangue and alteration minerals can occur. The complex compositions of tourmaline reflect changes in the chemical and physical environment during its formation, thus its chemical data can be combined with its morphology and stability over a wide range of conditions to make it well-suited to explore its formation conditions [4–6]. Tourmaline crystals have several characteristics in porphyry deposits as stated by [6]; such as oscillatory chemical zoning, the presence of several generations, Fe-Al substitution, and evolution from Fe-rich to Mg-rich varieties resulting from sulfide deposition. Moreover, the chemical data of tourmalines in porphyry Cu and Au deposits may indicate different stages of magmatic-hydrothermal processes, from the different exchange mechanisms, and distinguish early (potassic/propylitic) and late (phyllic) alteration. Tourmalines from the porphyry-copper deposits belong to the oxy-dravite–povondraite series [6].

Tourmaline occurrences related to porphyry Cu-Mo and Au deposits in Turkey were previously reported (Salikvan porphyry Cu-Mo deposit, NE Turkey: [7]; Kışladağ porphyry Au deposit: [8]). In the Salikvan deposit, tourmaline is located in quartz-tourmaline veins, tonalite porphyry to coarse granodiorite, and tourmaline-rich rocks at the contacts of coarse granodiorite and basic volcanic rocks. These tourmalines are relatively ferrous and calcic, showing a general trend from dravite to uvite end-members formed by the reaction of Fe-rich hydrothermal fluids with Ca-rich amphibole and plagioclase of the tonalite porphyry and granodiorite [7]. At the Kışladağ porphyry Au deposit, in which magmatic-hydrothermal brecciation is associated with multiphase intrusions of latite porphyry, tourmaline is an abundant and widespread alteration-induced mineral throughout the porphyry system. Two types of tourmaline occurrences are present in the Kışladağ deposit [8]. The first type occurs in the deeper levels of the deposit where tourmaline bearing veinlets occur in the potassic alteration zone (overprinting K-metasomatized rocks) and are composed mainly of quartz, pyrite, chalcopyrite, and tourmaline. The second type occurs in the matrix of hydrothermal breccias as disseminated radiating clusters and in discontinuous hairline veinlets with or without fine-grained quartz and pyrite. The tourmaline from Kışladağ belongs mainly to the alkali group with the representative Ca-rich buergerite composition deviating from the ideal schorl–dravite along a trend that closely approximates to the uvite exchange-vector [8]. In both instances, the tourmaline compositions have narrow ranges [7,8] that are similar to the composition of other well-known porphyry deposits [5–10].

The Kışladağ Au deposit, which is the subject of this study, is Europe's largest producing mine with different stages of mineralization occurring in the Miocene intrusive rocks (Figure 1). Tourmaline was developed in the Kışladağ porphyry gold deposit and associated with all phases of mineralization [11]. However, a detailed study has not been conducted as to whether tourmalines are associated with the porphyry system or whether there is tourmaline formation in a late-stage hydrothermal system rather than the porphyry system. Most of the tourmaline is present throughout the deposit as an outer alteration rim on veins, with lesser amounts disseminated in the intrusive host-rocks. The deposit consists of porphyry-style Au mineralization connected with a series of overlapping sub-volcanic monzonite intrusions (intrusive #1 to intrusive #3, [12]). In a recent study [13] related to fluid inclusions, it was proposed that the different quartz veins associations and the temperatures and salinities supported the process of an epithermal overprint of the primary porphyry mineralization.

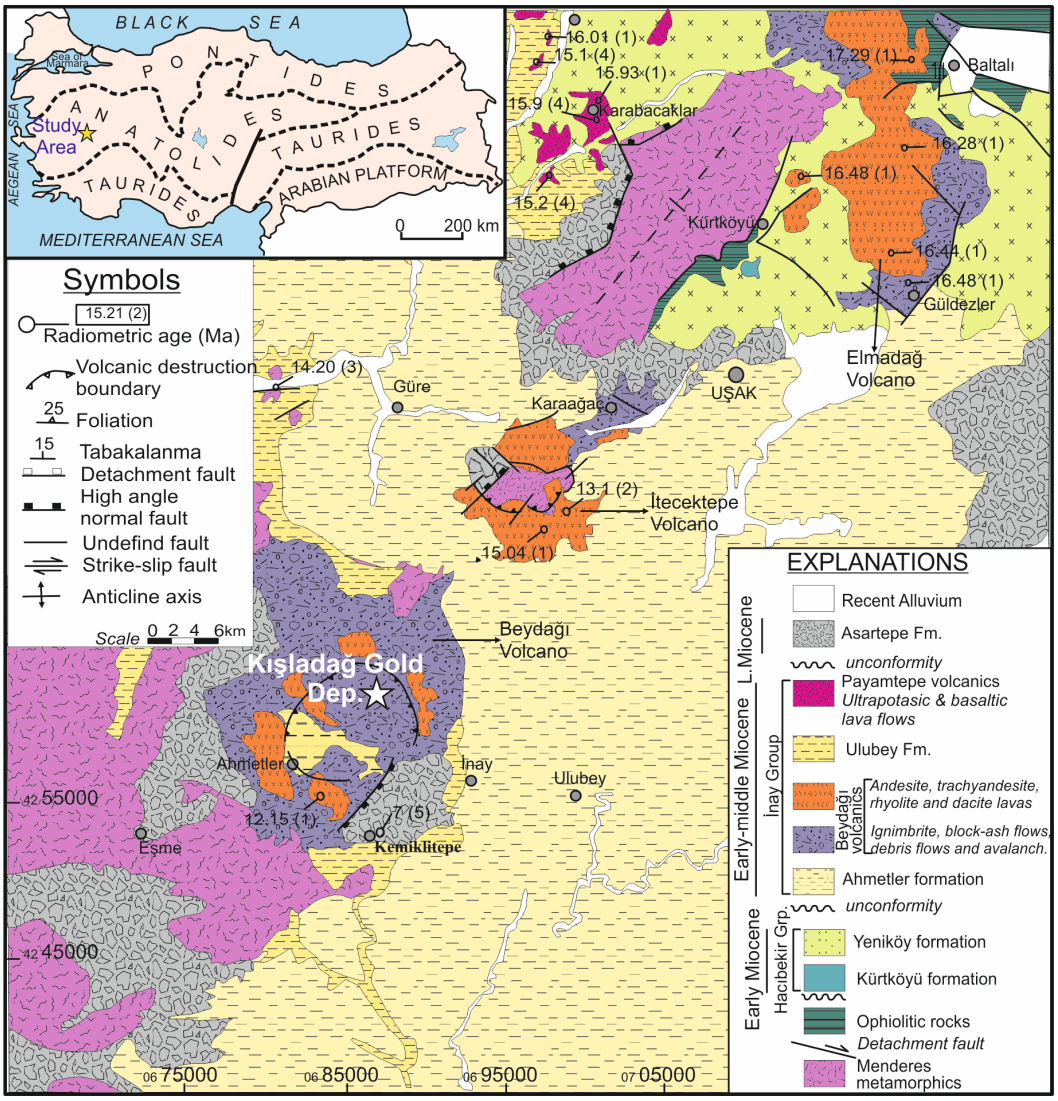

Figure 1. Geological map of the Uşak area [14] and location of the Kışladağ gold deposit.

This current study focuses on the tourmaline occurrences in the Kışladağ porphyry Au deposit to investigate the use of tourmaline by deciphering the physico-chemical conditions during the porphyry to epithermal transition, including late epithermal overprint.

2. Geological and Lithological Features

The Kışladağ deposit was the first porphyry-type Au mineralization discovered in Turkey. Early to Late Tertiary volcanic complexes related to the extensional tectonic regime in western Anatolia, occur in the study area [14]. These stratovolcanoes have been dated at between 17.29 Ma and 12.15 Ma by $^{40}Ar/^{39}Ar$ geochronology [14,15]. The Kışladağ porphyry Au deposit is related to monzonite intrusives and sub-volcanic rocks of the Beydağı volcanic complex with domes and intrusive bodies including andesite, latite, trachyte, dacite, rhyodacite, and rare basalt that intruded into the pre-Cretaceous Menderes metamorphic rocks [14,15].

The main geological and mineralization characteristics and fluid inclusion data of the deposit were given in previous studies [12,13,16,17]. The geological features of the Kışladağ deposit have been studied in detail by [12] and classified as an Au-only porphyry deposit due to the absence of significant amounts of Cu-mineralization. The main mineralized rocks of the deposit are intrusions of alkali affinity [16]. The intrusions are all monzonites, based on their mineralogical and chemical

compositions, and therefore have been subdivided according to their cross-cutting relationships [12], alteration, and mineralization. These are (i) intrusion #1 (INT#1), (ii) intrusion #2 (INT#2) and a more intense clay altered equivalent of intrusion #2 (INT#2A), and (iii) intrusion #3 (INT#3). All intrusions are mineralized but the most economically mineable Au mineralization occurs within the INT#1, INT#2, and INT#2A (Figure 2). The intrusions were emplaced into the metamorphic basement (Menderes metamorphics) and the older Beydağı volcanics.

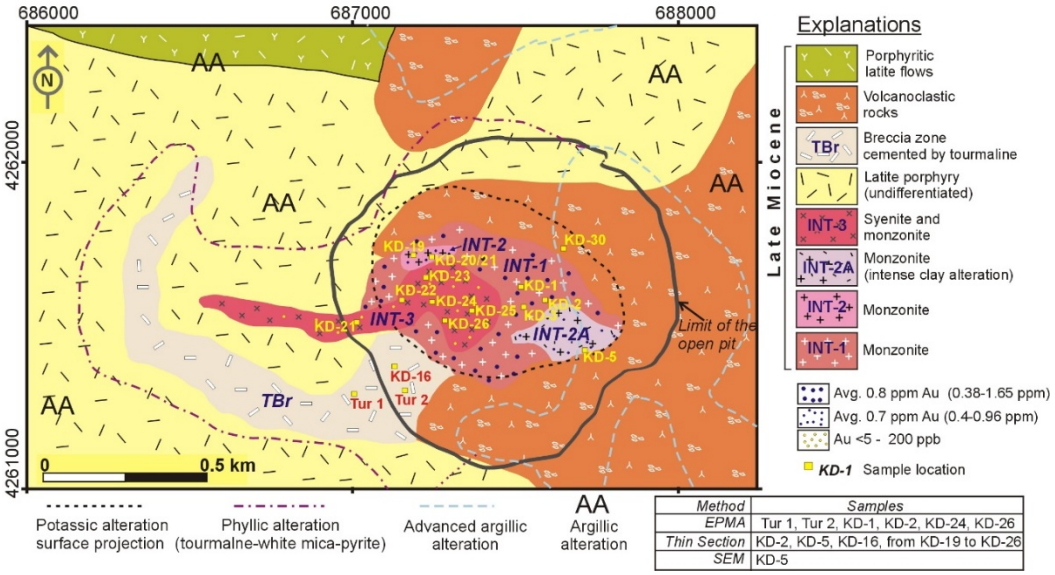

Figure 2. Lithological map of the Kışladağ Au deposit (modified after [16]; Au grades from [12]).

The metamorphic basement, represented by rocks of the Menderes Massif, is not exposed in the open pit but outcrops in the vicinity of the deposit, and has been intersected in the deep drillings. This comprises biotite-rich schists to highly quartz-bearing schists [12], composed mainly of quartz, plagioclase (albite), and white mica, with intensely deformed quartz veins.

The intrusive rocks (INT#1, INT#2/#2A, and INT#3) represent chronological order according to the relationship observed both at the surface and in drill core data [12,16].

INT#1 is the oldest and best mineralized intrusive phase in the Kışladağ mine area and forms the core of the system (Figure 2). It comprises abundant phenocrysts of K-feldspar, plagioclase, and biotite. Blocky megacryst(s) of K-feldspar, up to 1 cm, and rare quartz phenocrysts are characteristic of this unit [12,16]. INT#1 has a monzonitic character according to the primary mineral assemblages [16] and is cross-cut by the younger porphyritic intrusions. The contacts between INT#1 and the surrounding volcanic rocks are generally obscured by alteration.

INT#2 occurs in the center of the open pit, cutting the core of INT#1 (Figure 2), and contains coarse-grained (up to 2 mm in length) plagioclase phenocrysts in a dominantly K-feldspar groundmass. The INT#2 intrusion has a monzonite composition similar to INT#1. The INT#2A is a fine to medium-grained porphyritic rock, with intense pervasive kaolinite-illite-quartz (advanced argillic) alteration that appears to have selectively overprinted INT#2 and contains phenocrysts of plagioclase and rare quartz. Due to the similarity in the texture of INT#2 and INT#2A, both are believed to represent the same intrusion.

The INT#3 is the youngest intrusive body (Figure 2) and is a fine-grained porphyritic rock containing unaltered plagioclase phenocrysts, rare quartz, and biotite and amphibole phenocrysts. The bulk composition of INT#3 represents the composition of syenite-monzonite. The contacts of INT#3 with other rocks are generally well preserved, and the decrease in Au grade is abrupt.

The undifferentiated latite porphyry rocks cover a large area of the deposit site, especially west of the mineralized intrusions (Figure 2). These rocks contain large feldspar phenocrysts in a

fine-grained matrix of orthoclase and augite. The volcanoclastic rocks cover the mineralized intrusions, and outcrop in the east part of the study area (Figure 2). These exhibit different textures such as fine-grained fragmental ash fall tuffs with pumice fragments, to porphyritic flows with flow banding and brecciation. Due to the weak alteration, it is unclear whether the porphyries are intrusive bodies or flows. The contact between the volcanoclastics and INT#1 is difficult to define because of the intensity of alteration but is steeply inclined and often marked by a tourmaline rich hydrothermal breccia (Figures 2 and 3).

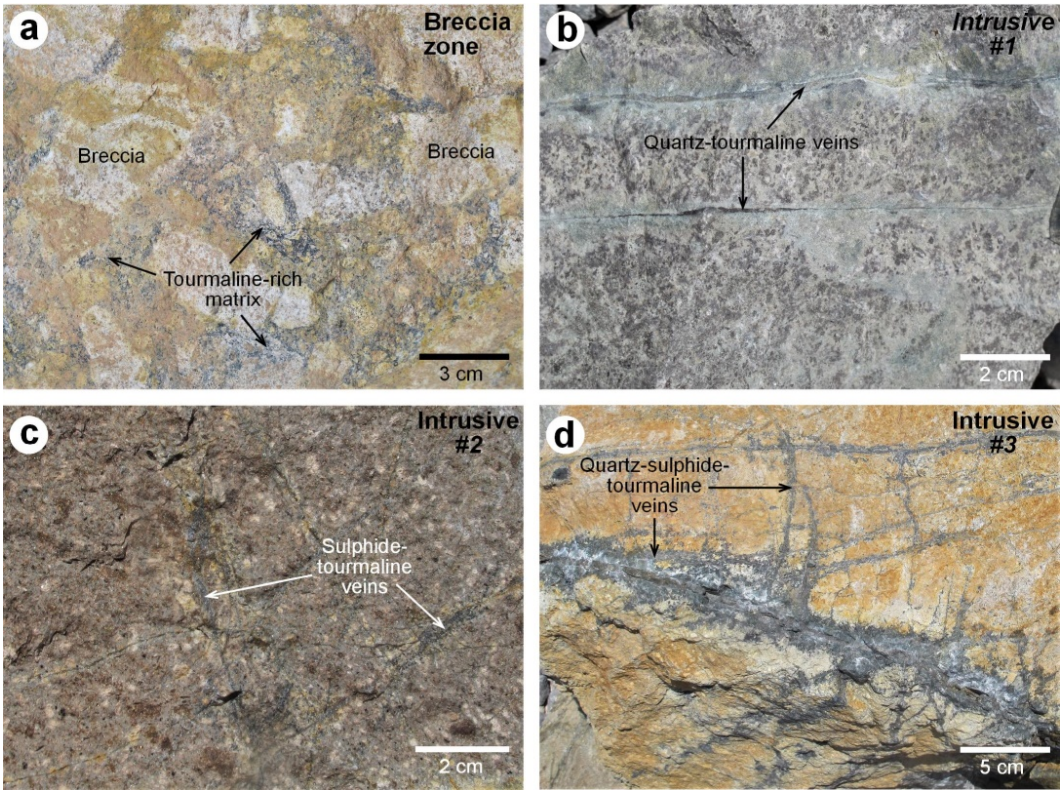

Figure 3. Macroscopic view of tourmaline bearing rocks from different zones (**a**) Tourmaline-rich matrix in breccia zone (TBZ) developed in latite porphyry, (**b**) Quartz-tourmaline vein crosscutting the potassic alteration in INT#1, (**c**) Sulfide-tourmaline veins crosscutting potassic alteration in INT#2, and (**d**) Quartz-sulfide-tourmaline veins crosscutting argillic alteration in INT#3.

3. Tourmaline Occurrences

Generally, porphyry-type mineralization systems have the classic potassic, phyllic, argillic (or advanced argillic in some deposits) and propylitic alteration zones (e.g., [18,19]), but only the potassic, tourmaline-white mica-pyrite (used as phyllic alteration in this study), advanced argillic and argillic alteration was developed in the Kışladağ deposit [12,16]. In terms of Au mineralization, tourmaline breccias are well mineralized where they contain coarse-grained clots of pyrite, but unmineralized intervals of tourmaline breccia are also present in the volcanic rocks.

The tourmaline-white mica-pyrite alteration is most intense surrounding the potassic zone within the deposit but also partially overlaps and overprints the potassic alteration [12]. Here, the tourmaline mineralization, which developed as a tourmaline-rich matrix in brecciated zones and tourmaline-quartz and/or tourmaline-sulfide veinlets within the different intrusive rocks, represents additional alteration products that are widely developed. This brecciated zone seems to have developed during the magmatic-hydrothermal brecciation related to the multiphase effects of intrusions over a period of approximately 5 Ma [12]. Tourmaline exists throughout the deposit and in all phases associated with the three intrusions except for late vuggy silica which is associated with the advanced argillic

alteration in volcanoclastic rocks [16], which is most common in volcanic rocks adjacent to INT#1 forming an outer alteration shell (Figure 2). The stockworks containing Au are commonly associated with tourmaline-quartz veins, banded quartz-pyrite-tourmaline veins that are cut by sooty pyrite ± marcasite–tourmaline veins [12,13,16].

Tourmaline-bearing brecciated zones occur in the tourmaline-white mica-pyrite alteration (phyllic) zone, surrounds the potassic zone (Figure 2), and are overprinted by an advanced argillic assemblage, characterized mainly by alunite occurrences [16]. Within the intrusions (INT#1 to INT#3), tourmaline commonly occurs as envelopes around quartz ± pyrite veinlets, grading into black quartz-tourmaline matrix-supported hydrothermal breccias containing angular fragments of wall rock (Figure 3a) and as envelopes around the quartz veinlets (Figure 3b). Tourmalines are commonly associated with the sulfide (pyrite ± marcasite) and quartz minerals in the veins as seen within the INT#2 and INT#3 (Figure 3c,d). The widths of tourmaline-rich matrix zones range from 0.5 to 2 cm (Figure 3a), but tourmaline-rich zones have a thickness of less than 0.5 cm in quartz and quartz-sulfide veinlets (Figure 3b–d). Tourmaline alteration in the volcanic rocks through crosscutting breccia bodies is also present and typically occurs as microcrystalline masses giving the rock a blue-green color [12].

4. Materials and Methods

Scanning electron microscope (SEM) secondary (SE) and backscattered electron (BSE) images of tourmaline bearing samples were obtained with a JEOL JSM-7600F at Muğla Sıtkı Koçman University (Muğla, Turkey) and a Carl Zeiss Supra 40 VP Field Emission Scanning Electron Microscope at Pamukkale University (Denizli, Turkey). The majority of the electron microprobe data from tourmaline was obtained using a JEOL JSM-6480LV electron microscope equipped with an Inca Energy-350 energy dispersion system (EDS) and Inca Wave-500 wavelength dispersion system (WDS) at the Laboratory of Analytical Techniques of High Spatial Resolution, Department of Petrology, Moscow State University, analyst N.N. Korotaeva. The JEOL JSM-6480LV electron microscope was operated at an accelerating voltage of 15 kV and a beam current of 20 nA. The EDS detector was used for all elements except F, employing natural silicate reference minerals [20] for calibration. The uncertainty of single measurements of oxides did not exceed 1.5%. Fluorine concentrations were measured with WDS (TAP crystal), using MgF2 as a reference standard. The XPP (eXtended Pouchou and Pichoir) corrections were used for corrections (program "INCA" version 17a).

Tourmaline formulae were calculated on the basis of 15 cations at the tetrahedral and octahedral sites (T, Z, and Y) exclusive of Na, Ca, and K, which is appropriate for low-Li tourmaline as expected in rocks of the type studied here [3]. Total iron was assumed to be Fe^{2+}. Charge-balance constraints were used to estimate the amounts of OH^{-} and O^{2-} in the V and W anion sites. We recognize that there are significant uncertainties with these estimates [21]. The proportion of X-site vacancies (□) was calculated as [1 − (Na + Ca + K)]. The concentration of B_2O_3 was calculated from stoichiometric constraints assuming 3 atoms per formula unit (a.p.f.u.) B. Iron is reported as both Fe^{2+} and Fe^{3+} when Mössbauer spectra were taken from the literature [8], in other instances Fe is given as Fe^{2+}.

5. Results

5.1. Tourmaline-Breccia Zone (TBZ)

The radial tourmaline aggregates (rosettes) of about several hundred micrometers in diameter are optically zoned (Figure 4a); they exhibited a dark green or brown-green core and light yellow-green rim. The tourmaline core is strongly pleochroic, from green to nearly black, indicating the presence of iron in both valences. The aggregate rim is weakly pleochroic testifying to the predominance of one of two iron valences. The tourmaline aggregates are commonly corroded by quartz crystals, which occur as pore or vein-fillings in the TBZ. The back-scattered electron images (BSE) (Figure 4b,c) showed a much more complex pattern caused by the variable chemical composition. In the radial aggregates (image center) the BSE color of tourmaline evolves from a white core (probably enriched in Fe) through

greyish white, light grey to dark grey (probably depleted in Fe). It is worth noting that a similar color evolution is observed in relatively large crystals (upper right corner of the image). In this case, the color (resulting from the composition variation) evolves from dark grey through light grey to dark grey again. Summarizing these observations, the following general crystallization sequence of tourmaline can be proposed: white tourmaline (tourmaline I) → grey (tourmaline II) tourmaline → light grey to whitish-grey tourmaline (tourmaline III) → dark grey (tourmaline IV). It should be noted that within each of these four zones there is additional oscillatory zoning with darker and lighter subzones.

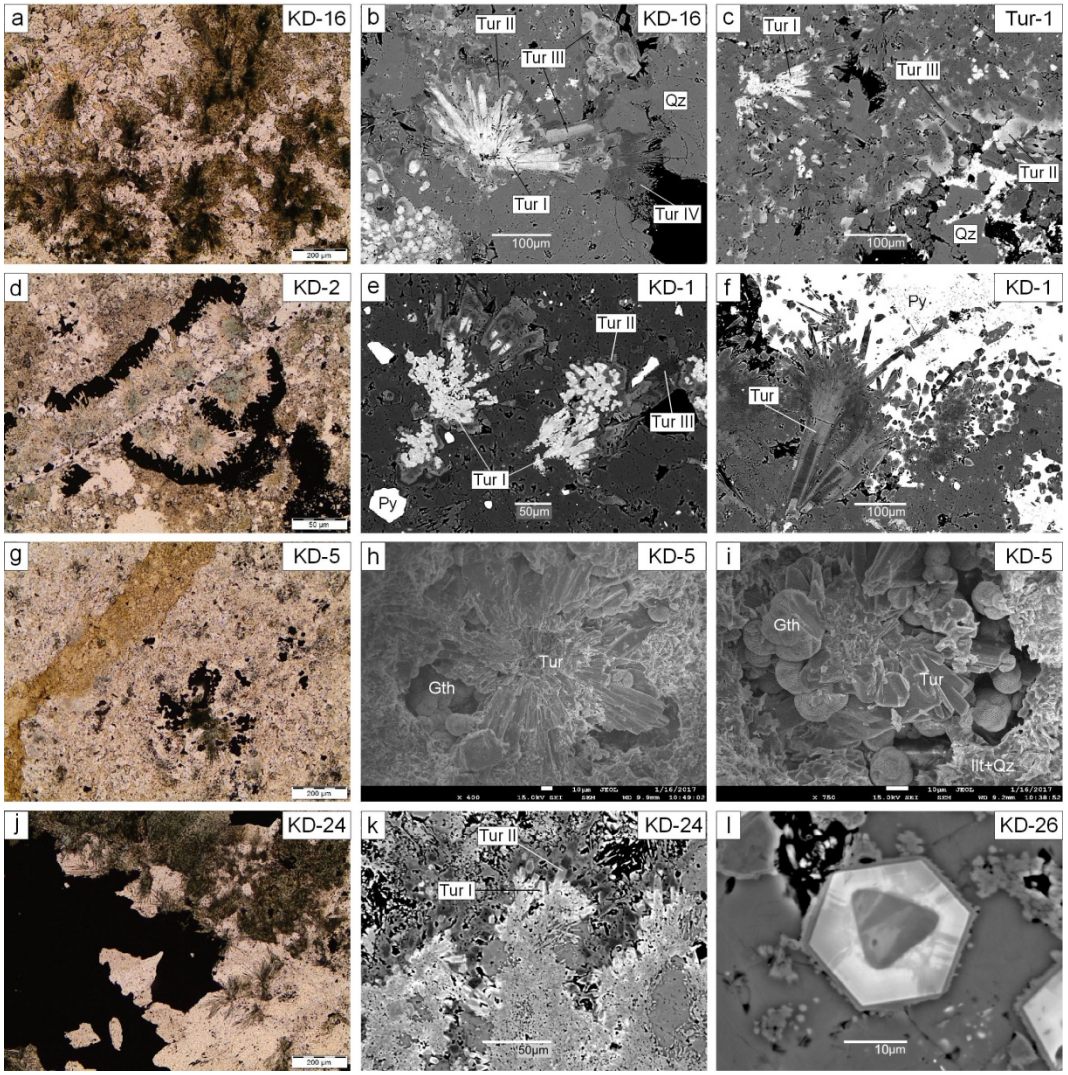

Figure 4. Optical photomicrographs, scanning electron microscope secondary electron and back-scattered electron images of tourmaline from the Kışladağ deposit. (**a**–**c**) Tourmaline breccia zone (TBZ): (**a**) optically zoned fine-acicular radial aggregate, (**b**) zoned radial aggregates composed of several tourmaline generations (image center) and aggregate of relatively large zoned crystals filling cavity (right top angle of image), (**c**) radial aggregate of tourmaline I and relatively large zoned crystals; (d–f) INT#1: (**d**) optically zoned rosette of tourmaline rimed by opaque (sulfide) minerals (black), (**e**) zoned radial aggregate composed of several tourmaline generations, (**f**) zoned tourmaline crystal with divergent tip; (**g**–**i**) INT#2A: tourmaline rosettes in association with goethites filling cavities within the intensely illite altered-silicified porphyry rock; (**j**–**l**) INT#3: (**j**) radial weakly optically zoned tourmaline aggregates in quartz at the contact with sulfide pocket (black), (**k**) fine-acicular zoned aggregate of tourmaline, (**l**) euhedral complexly zoned tourmaline crystal. Gth: goethite; Ilt: illite; Py: pyrite; Qz: quartz; Tur: tourmaline.

According to structural formula calculations, the Y site in the tourmaline I is dominated by Fe or Mg (Table 1). On a triangular plot X-vacancy–Ca–Na(+K), tourmaline compositions fall into all three fields (Figure 5a).

Table 1. Chemical composition of tourmaline from the TBZ.

Component, wt %	Radial Aggregates				Crystal
	Tur I (*n* = 16)	**Tur II (*n* = 14)**	**Tur III (*n* = 12)**	**Tur IV (*n* = 9)**	**(*n* = 7)**
B_2O_3	10.22 (0.14) *	10.77 (0.22)	10.91 (0.17)	10.85 (0.11)	10.86 (0.18)
SiO_2	34.43 (0.65)	36.74 (0.95)	37.38 (0.67)	35.75 (1.63)	37.13 (0.66)
TiO_2	0.33 (0.32)	1.52 (1.23)	1.25 (1.29)	0.28 (0.52)	1.14 (0.97)
Cr_2O_3	0.01 (0.02)	0.13 (0.20)	0.02 (0.02)	*bdl*	*bdl*
V_2O_3	0.06 (0.06)	0.39 (1.00)	0.09 (0.03)	*bdl*	*bdl*
Al_2O_3	25.53 (2.45)	30.48 (3.14)	32.06 (3.05)	37.21 (2.49)	32.51 (3.66)
FeO_{tot}	15.47 (3.33)	4.83 (3.49)	3.12 (3.72)	1.20 (0.95)	3.41 (2.75)
MnO	0.05 (0.04)	0.04 (0.05)	0.04 (0.08)	0.02 (0.04)	*bdl*
MgO	6.98 (0.92)	9.82 (1.64)	10.27 (0.66)	8.57 (1.08)	9.76 (0.65)
CaO	2.13 (0.31)	2.12 (0.63)	1.37 (0.94)	1.11 (0.47)	1.29 (0.65)
K_2O	0.05 (0.02)	0.03 (0.02)	0.03 (0.03)	*bdl*	0.03 (0.04)
Na_2O	1.43 (0.16)	1.49 (0.18)	1.78 (0.26)	1.06 (0.43)	1.74 (0.13)
F	0.02 (0.04)	0.06 (0.09)	0.14 (0.09)	0.09 (0.07)	*n.a.*
Cl	0.06 (0.04)	0.04 (0.06)	*bdl*	0.11 (0.10)	*bdl*
H_2O	2.97 (0.09)	3.41 (0.20)	3.44 (0.24)	3.42 (0.35)	3.48 (0.09)
2F=O	0.01 (0.01)	0.03 (0.04)	0.06	0.04 (0.03)	
2Cl=O	0.01 (0.01)	0.01 (0.01)		0.03 (0.02)	
Total	99.70 (0.63)	102.30 (1.19)	101.86 (0.82)	99.62 (2.18)	101.32 (0.82)
Si	5.854	5.927	5.955	5.727	5.944
^{T}Al	0.146	0.073	0.045	0.273	0.056
Total T	6.000	6.000	6.000	6.000	6.000
^{Z}Al	4.969	5.722	5.975	6.000	6.000
^{Z}Mg	1.031	0.278	0.025		
Total Z	6.000	6.000	6.000	6.000	6.000
Fe^{3+}	1.321				
Fe^{2+}	0.880	0.653	0.416	0.161	0.456
^{Y}Al				0.755	0.078
^{Y}Mg	0.739	2.085	2.415	2.046	2.329
Ti	0.042	0.191	0.149	0.034	0.137
Mn	0.007	0.005	0.006	0.003	
V	0.008	0.050	0.011		
Cr	0.002	0.017	0.003		
Total Y	2.999	3.001	3.000	2.999	
Na	0.470	0.465	0.551	0.331	0.539
Ca	0.389	0.367	0.235	0.190	0.221
X-vacancy	0.131	0.161	0.208	0.479	0.234
K	0.010	0.006	0.007		0.006
Total X	1.000	1.000	1.000	1.000	1.000
$^{V}OH^{-}$	3.000	3.000	3.000	3.000	3.000
$^{W}O^{2-}$	0.495	0.286	0.266	0.261	0.283
$^{W}OH^{-}$	0.374	0.670	0.662	0.660	0.717
Cl	0.017	0.012		0.030	
F	0.009	0.032	0.072	0.047	
Total W	1.000	1.000	1.000	1.000	1.000
Al_{tot}	5.115	5.795	6.020	7.027	6.134
Fe_{tot}	2.201	0.653	0.416	0.161	0.456
Mg_{tot}	1.770	2.363	2.440	2.046	2.329

Fe^{2+} and Fe^{3+} in tourmaline I are calculated using the Mössbauer data from [8]. Cations between the Z and Y sites were distributed according to [3]. FeO_{tot} = Total FeO, *bdl*= below detection limit, *n.a.*= not analyzed. * Numerals in parenthesis are standard deviations.

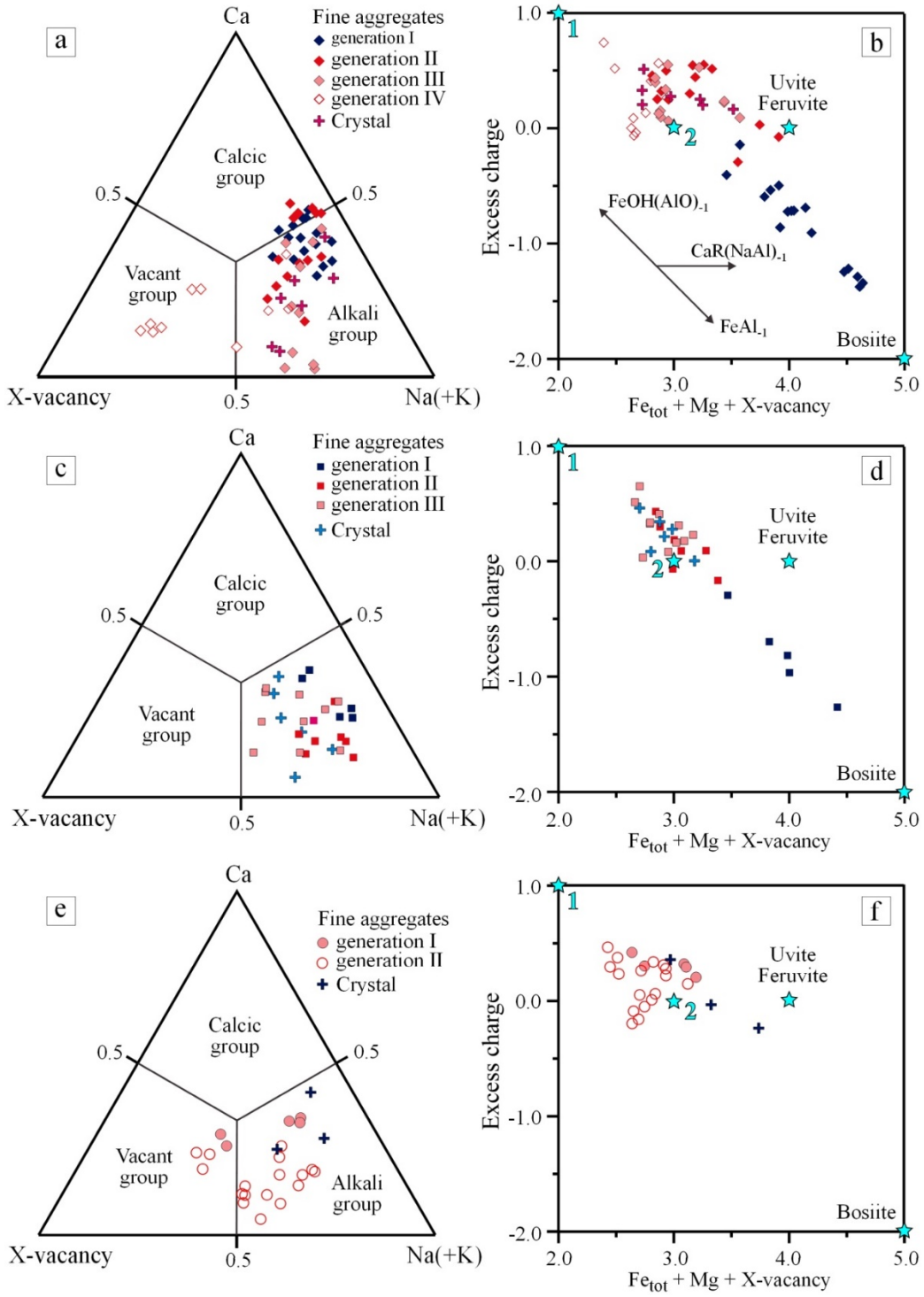

Figure 5. Triangular X-site vacancy–Ca–Na(+K) and binary excess charge versus Fe_{tot} + Mg + X-vacancy diagrams illustrating tourmaline compositions from (**a**,**b**) TBZ, (**c**,**d**) INT#1, and (**e**,**f**) INT#3. Stars indicate the tourmaline end-members. (1) X-vacancy—R^{2+}–O rootname (oxy-magnesio-foitite) and oxy-foitite, (2) schorl, dravite, magnesio-foitite, foitite.

According to structural formula calculations, the Y site in the tourmaline I is dominated by Fe or Mg (Table 1). On the binary plot excess charge versus Fe_{tot} + Mg + X-vacancy (Figure 5b), the tourmaline I compositions are below schorl–dravite point and are parallel to the $FeAl_{-1}$ exchange vector that corresponds to the $Fe^{3+} \leftrightarrow$ Al substitution. Some compositions of tourmaline I compositions are close to the bosiite point on this diagram implying the high Fe^{3+} in the mineral.

On the X-vacancy versus the Ca diagram, no clear compositional trend is observed from tourmaline I (Figure 6a). Correlation coefficients between Ca and Na and Ca and X-site vacancy in tourmaline I were −0.69 and −0.37, respectively. This suggests Ca-Na and Ca-X-site vacancy exchanges with a predominant Ca–Na exchange. According to [22], this exchange implies Ca + R^{2+} → Na + Al, Ca + O → Na + OH, and Ca + $2R^{2+}$ + OH → Na + 2Al + O. Correlation coefficients between Ca + O and Na + OH and Ca + $2Fe^{2+}$ + OH and Na + 2Al + O were −0.91 and −0.90, respectively. In the case of Mg as the divalent cation, the correlation coefficient is 0.15. These values suggest two probable substitutions of Ca + O → Na + OH, and Ca + $2R^{2+}$ + OH → Na + 2Al + O in the tourmaline compositions. On the Fe–Al–Mg triangular diagram (Figure 6b), the tourmaline I compositions are roughly parallel to the oxy-dravite bosiite trend. Considering these observations, tourmaline I could be classified as the intermediate member of the oxy-dravite bosiite solid solution series enriched in Ca; some tourmaline compositions belong to the calcic species. We do not have Mössbauer data from these, however; Oyman and Dyar [8] reported that the Fe^{3+}/Fe_{tot} ratio in the breccia-zone tourmaline is 0.60. If the tourmaline I formulas are calculated with this Fe^{3+}/Fe_{tot} value then they would be classified as dravite, oxy-dravite, schorl, oxy-schorl, bosiite, feruvite, and magnesio-lucchesiite. All compositions show enrichment in ferric iron; dravite, oxy-dravite, schorl, oxy-schorl, and bosiite are enriched in Ca. Using the Oyman and Dyar [8] data, the calculated correlation coefficients between Al and Fe^{3+}, Fe^{2+} and Mg, Fe^{2+} + ^{W}OH, and Al_{tot} + ^{W}O were −0.84, −0.99, −0.91. These values indicate that Fe^{2+} incorporates into the tourmaline structure according to Fe^{2+} → Mg and Fe^{2+} + ^{W}OH → Al_{tot} + ^{W}O. The first substitution is slightly preferable. Ferric iron incorporates according to Al → Fe^{3+}.

Thus, tourmaline I is extremely variable in composition and is classified as dravite, oxy-dravite, schorl, oxy-schorl, bosiite, feruvite, and magnesio-lucchesiite. It is distinguished by Fe^{3+} → Al, Fe^{2+} → Mg, Fe^{2+} + ^{W}OH → Al_{tot} + ^{W}O, Ca + O → Na + OH, and Ca + $2Fe^{2+}$ + OH → Na + 2Al + O substitutions.

Calculated formulas of tourmaline II–IV indicated that the Y site is dominated by Mg (Table 1). On the binary plot excess charge versus Fe_{tot} + Mg + X-vacancy (Figure 5b), tourmaline compositions are between dravite, X-vacancy-Mg-O root name ("oxy-magnesio-foitite"), and uvite, or between two exchange vectors $FeAl_{-1}$ and $CaR(NaAl)_{-1}$, where R = Mg, Fe^{2+}. Such a position indicates an insignificant proportion of Fe^{3+} in the tourmaline composition. This is supported by the charge balance, which does not require Fe^{3+}, except for two compositions of tourmaline II and one of tourmaline IV. On the binary plot, X-site vacancy versus Ca (Figure 6a), the compositions of tourmalines II and III are nearly parallel to the exchange vectors: $CaR_2\square_{-1}Al_{-2}$, $CaRO\square_{-1}Al_1(OH)_{-1}$, and $CaR_3(OH)\square_{-1}Al_{-3}O_{-1}$, where R = Fe^{2+}, Mg.

Correlation coefficients (Table 2) indicate that Ca + Mg + ^{W}O → X-vacancy + Al + ^{W}OH and Ca + Fe^{2+} + ^{W}O → X-vacancy + Al + ^{W}OH were major substitutions in tourmaline II, whereas in tourmaline III, these were Ca + 2Fe → X-vacancy + 2Al and Ca + Fe^{2+} +^{W}O → X-vacancy + Al + ^{W}OH. Considering the calculated formulas, tourmaline II can be classified as dravite, oxy-dravite, uvite, and magnesio-lucchesiite, whereas tourmaline III was oxy-dravite and dravite. Tourmaline II was characterized by Ca + Mg +^{W}O → X-vacancy + Al + ^{W}OH and Ca + Fe^{2+} +^{W}O → X-vacancy + Al + ^{W}OH substitution, whereas in tourmaline III, Ca + 2Fe → X-vacancy + 2Al and Ca + Fe^{2+} + ^{W}O → X-vacancy + Al + ^{W}OH.

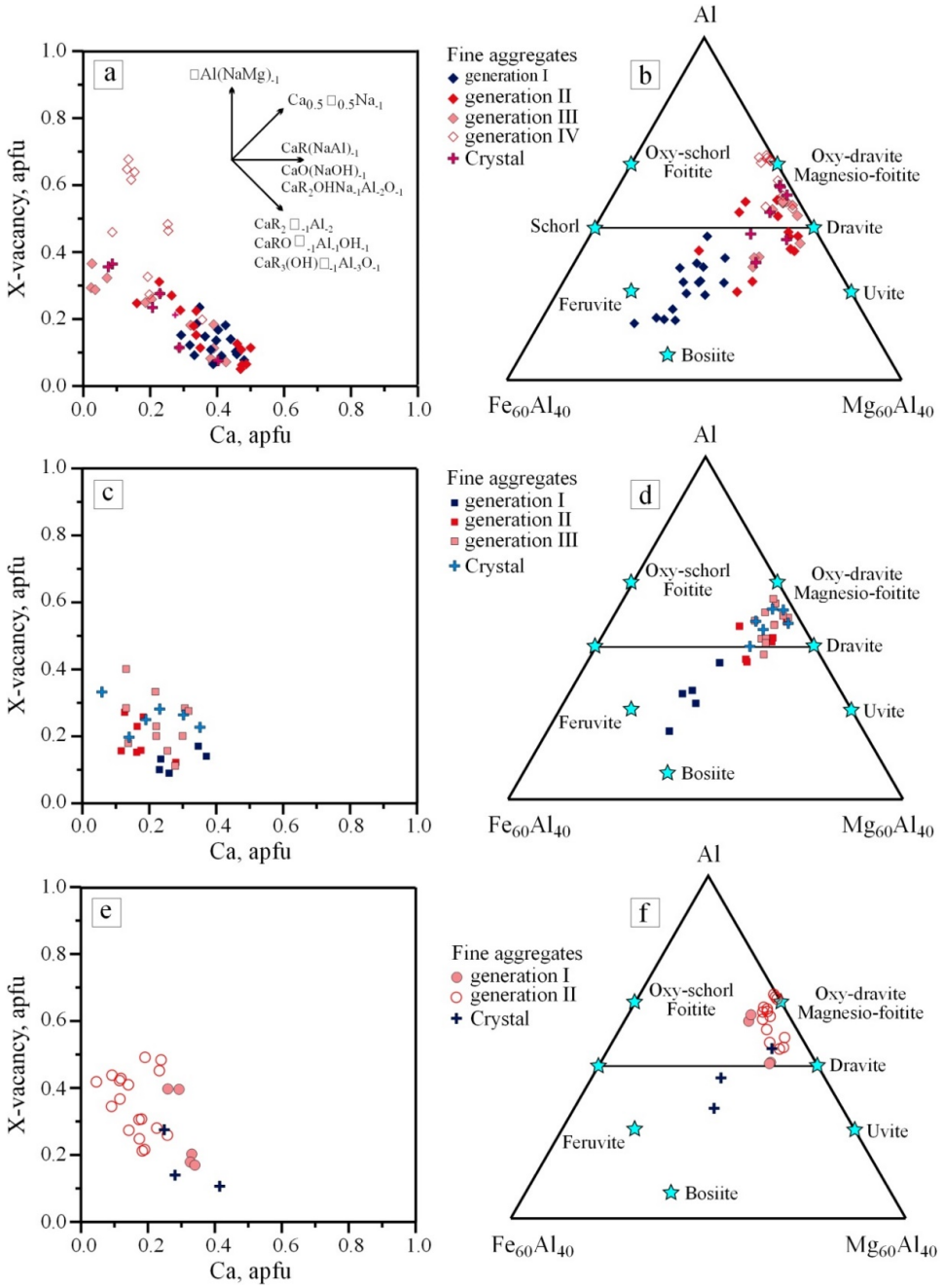

Figure 6. Binary X-vacancy versus Ca and triangular Fe–Al–Mg diagrams illustrating tourmaline compositions from (**a**,**b**) TBZ, (**c**,**d**) INT#1, and (**e**,**f**) INT#3. Stars indicate the tourmaline end-members.

Table 2. Correlation coefficients for tourmalines II and III.

Correlation Type	II	III
Ca + 2Mg and X-vacancy + Al	−0.42	−0.49
Ca + Mg + ^{W}O and X-vacancy + Al + ^{W}OH	−0.73	−0,71
Ca + 3Mg + ^{W}OH and X-vacancy + 3Al + ^{W}O	−0.62	−0.46
Ca + 2Fe$_{tot}$ and X-vacancy + 2Al	−0.62	−0.92
Ca + Fe$_{tot}$ + ^{W}O and X-vacancy + Al + ^{W}OH	−0.75	−0.95
Ca + 3Fe$_{tot}$ + ^{W}OH and X-vacancy + 3Al + ^{W}O	−0.60	−0.89

The compositions of tourmaline IV fall into the X-vacant and alkali fields on the triangular plot X-site vacancy–Ca–Na(+K) (Figure 5a) that allows for their attribution to the X-vacant and alkali tourmalines. In contrast to tourmalines II and III, the compositions of tourmaline IV were nearly parallel to the $\square Al(NaR)_{-1}$ exchange vector on the X-vacancy versus Ca diagram (Figure 6a) that implies X-site vacancy + Al → Na + R substitution, where R = Mg, Fe^{2+}.

The correlation coefficients between X-site vacancy + Al and Na + Mg and X-site vacancy + Al and Na + Fe were −0.90 and −0.85. These values show that isomorphic substitution involving Mg is preferred. Considering the calculated formulas, tourmaline IV can be classified as magnesio-foitite, X-vacancy-Mg-O root name (oxy-magnesio-foitite), dravite, and oxy-dravite with the major substitution X-site vacancy + Al and Na + Mg, in accordance with [22]. An interesting feature of tourmaline IV is the elevated chlorine content, which was between 0.13 to 0.26 wt %.

Based on their composition the relatively large tourmaline crystals classifies these as dravite with one being oxy-dravite. The analyses in Table 1, indicates the chemical composition of the relatively large tourmaline is similar to tourmaline III. In addition, both plot in similar positions in Figures 5a and 6a. Therefore, a simultaneous crystallization of tourmaline III and the relatively large tourmaline crystals was likely.

On a triangular plot, $Fe_{60}Al_{40}$–Al_{tot}–$Mg_{60}Al_{40}$ (Figure 6b), the compositions of tourmalines in the breccia zone are above and slightly below the schorl–dravite line. Their position below this line may imply enrichment in Fe^{3+}. In the case of tourmaline I, this is supported by the Mössbauer data from [8] and calculations from this current study. For some tourmaline II and III compositions, which are probably depleted in ferric iron, their location is caused by slight depletion in Al.

Thus, tourmalines I, II, III, and IV from the breccia zone are different in isomorphic substitutions, as well as, in Fe^{3+} and Na contents, evolving in general from Fe^{3+}-rich alkali to Fe-poor X-vacant species. Tourmaline IV is enriched in chlorine. The relatively large tourmaline crystals are possibly synchronous with the tourmaline III radial aggregates.

5.2. Intrusion #1 (INT#1)

The tourmaline here is morphologically similar to the TBZ, occurring as radial aggregates of up to 50 micrometers in diameter with a green core and colorless or yellowish rim (Figure 4d). The core of the tourmaline is strongly pleochroic from green to dark green, whereas tourmaline from the rim varies from colorless to pale green. Electron microscopy revealed that zoning of radial aggregates was again similar to the radial tourmaline aggregates from the TBZ (Figure 4e): (1) white (tourmaline I) → grey and light grey (tourmaline II) → dark grey and grey (tourmaline III) and (2) grey → dark grey → white → grey. In addition, zoned crystals up to 200 μm long with divergent tips were present (Figure 4f). The zoning in these crystals is from: whitish-grey → dark grey → grey → nearly black, with only a single generation present.

On the triangular plot of X-vacancy–Ca–Na(+K), tourmaline compositions fall into the alkali field (Figure 5c). Based on calculations, the Y site in tourmaline I radial aggregates were dominated by Fe (Table 3). On the binary plot, excess charge versus Fe_{tot} + Mg + X-vacancy (Figure 5d), the tourmaline I compositions were below the schorl–dravite line and parallel to the $FeAl_{-1}$ exchange vector that corresponds to the Fe^{3+} → Al substitution.

The tourmaline I compositions were identical to the tourmaline I compositions from the TBZ, with the same explanation for the high proportion of Fe^{3+}. On the Fe–Al–Mg triangular diagram, the tourmaline I compositions are roughly parallel to the oxy-dravite-bosiite trend. Therefore, tourmaline I could be classified as the intermediate member of the oxy-dravite-bosiite solid solution series enriched in Ca.

Table 3. Chemical composition of tourmaline from INT#1.

Component, wt %	Radial Aggregate			Crystal
	Tur I (*n* = 5)	**Tur II (*n* = 7)**	**Tur III (*n* = 8)**	**(*n* = 6)**
B_2O_3	10.34 (0.10)	10.86 (0.12)	10.80 (0.16)	10.93 (0.13)
SiO_2	34.76 (0.79)	37.29 (0.82)	36.69 (0.91)	37.08 (0.67)
TiO_2	0.41 (0.30)	0.45 (0.51)	0.61 (0.46)	0.31 (0.13)
Cr_2O_3	*bdl*	*bdl*	*bdl*	*bdl*
V_2O_3	0.07 (0.08)	0.09 (0.06)	0.22 (0.29)	0.03 (0.04)
Al_2O_3	26.49 (2.34)	32.30 (1.64)	33.08 (2.19)	34.20 (1.65)
FeO_{tot}	14.88 (2.97)	4.93 (2.46)	4.02 (1.33)	3.43 (2.14)
MnO	0.27 (0.13)	0.05 (0.10)	bdl	0.02 (0.03)
MgO	6.83 (0.46)	9.26 (0.90)	9.11 (0.41)	9.26 (0.71)
CaO	1.59 (0.37)	1.00 (0.31)	1.46 (0.34)	1.24 (0.62)
K_2O	*bdl*	*bdl*	*bdl*	*bdl*
Na_2O	1.79 (0.27)	2.05 (0.20)	1.68 (0.31)	1.72 (0.31)
F	*n.a.*	*n.a.*	*n.a.*	*n.a.*
Cl	*bdl*	*bdl*	*bdl*	0.01 (0.01)
H_2O	3.56 (0.04)	3.43 (0.13)	3.47 (0.09)	3.54 (0.13)
2F=O				
2Cl=O				0.03 (0.01)
Total	100.99 (0.41)	101.66 (0.84)	100.66 (1.02)	101.78 (0.85)
Si	5.844	5.967	5.901	5.896
^{T}Al	0.156	0.033	0.099	0.104
Total T	6.000	6.000	6.000	6.000
^{Z}Al	5.094	6.000	6.000	6.000
^{Z}Mg	0.906			
Total Z	6.000	6.000	6.000	6.000
Fe^{3+}	0.790			
Fe^{2+}	1.303	0.660	0.542	0.456
^{Y}Al		0.059	0.172	0.305
^{Y}Mg	0.806	2.209	2.184	2.195
Ti	0.052	0.054	0.073	0.037
Mn	0.038	0.006		0.003
V	0.010	0.012	0.028	0.003
Cr				
Total Y	2.999	3.000	2.999	2.999
Na	0.584	0.635	0.523	0.530
Ca	0.287	0.171	0.253	0.211
X-vacancy	0.129	0.194	0.224	0.259
K				
Total X	1.000	1.000	1.000	1.000
$^{V}OH^{-}$	3.000	3.000	3.000	3.000
$^{W}O^{2-}$		0.332	0.276	0.232
$^{W}OH^{-}$	1.000	0.668	0.724	0.760
Cl				0.008
F				
Total W	1.000	1.000	1.000	1.000
Al_{tot}	5.250	6.092	6.271	6.410
Fe_{tot}	2.094	0.660	0.444	0.456
Mg_{tot}	1.712	2.209	2.184	2.195

Fe^{2+} and Fe^{3+} calculated from charge balance constraints. *bdl* = below detection limit, *n.a.* = not analyzed.

The average chemical compositions of tourmaline I from the TBZ and INT#1 are similar (Table 3). In view of this fact and position of the tourmaline I compositions from INT#1 on the excess charge versus Fe_{tot} + Mg + X-vacancy plot (Figure 5d), we suggest the same isomorphic substitutions as those in tourmaline I from the TBZ: $Fe^{2+} \rightarrow Mg$, $Fe^{2+} + {}^{W}OH \rightarrow Al_{tot} + {}^{W}O$, and $Al \rightarrow Fe^{3+}$.

On the binary plot X-site vacancy versus Ca (Figure 6c), the compositions of tourmaline I are arranged like those of tourmaline I from the TBZ. We have only five compositions for tourmaline I, from this intrusion, therefore correlation coefficients have a greater possible error. However, the similar arrangement of tourmaline I from the INT#1 and TBZ would be consistent with the same isomorphic substitutions in the intrusion tourmaline I, i.e., Ca + O → Na + OH and $Ca + 2Fe^{2+} + OH \rightarrow Na + 2Al + O$. The calculated formulas of tourmaline II and III indicate that the Y site is dominated by Mg (Table 3).

In the binary plot excess charge versus Fe_{tot} + Mg + X-vacancy (Figure 5d), all but two of the compositions are between dravite and "oxy-magnesio-foitite" or nearly parallel to the $AlO(R(OH))_{-1}$ exchange vector, where R = Mg, Fe^{2+}. Such a position indicates an insignificant concentration of Fe^{3+} in the tourmaline. This is supported by the charge balance, which does not require Fe^{3+} except for two compositions of tourmaline II. The significant correlation coefficients of −0.85 and −0.93 were calculated for $Fe + {}^{W}OH^{-}$ and $Al + {}^{W}O^{2-}$ for tourmaline II and between $Mg + {}^{W}OH^{-}$ and $Al + {}^{W}O^{2-}$ for tourmaline III, respectively. These values indicate different coupled substitution in these tourmalines, $Fe + {}^{W}OH^{-} \leftrightarrow Al + {}^{W}O^{2-}$ and $Mg + {}^{W}OH^{-} \leftrightarrow Al + {}^{W}O^{2-}$, respectively.

On the binary plot X-site vacancy versus Ca (Figure 6c), the compositions of tourmalines II and III are nearly parallel to the exchange vectors: $CaR_2\square_{-1}Al_{-2}$, $CaRO\square_{-1}Al_{-1}(OH)_{-1}$, and $CaR_3(OH)\square_{-1}Al_{-3}O_{-1}$, where R = Fe^{2+}, Mg.

The highest correlation coefficient (−0.74) for the tourmaline II compositions was calculated between $Ca + 3Fe + {}^{W}OH$ and $\square + 3Al + {}^{W}O$ implying $Ca + 3Fe + {}^{W}OH \leftrightarrow \square + 3Al + {}^{W}O$ substitution. However, for the seven Tur II analyses (Table 3) this is not sufficiently significant to be sure this substitution is correct. The highest correlation coefficient (−0.97) for eight tourmaline III compositions was calculated between $Ca + 3Mg + {}^{W}OH$ and X-vacancy + $3Al + {}^{W}O$. This implies the $Ca + 3Mg + {}^{W}OH \leftrightarrow$ X-vacancy + $3Al + {}^{W}O$ substitution. According to calculations, the tourmaline of the zoned crystals is classified as dravite with one as oxy-dravite. The analyses in Table 3 shows the average chemical composition of this tourmaline is similar to that of tourmaline III. In addition, on the X-site vacancy–Ca–Na and X-site vacancy versus Ca diagrams (Figures 5c and 6c), the composition arrangement of large crystals and tourmaline III is similar. Therefore, simultaneous crystallization of tourmaline III and zoned tourmaline crystals are likely.

On a triangular plot of $Fe_{60}Al_{40}$–Al_{tot}–$Mg_{60}Al_{40}$ (Figure 6d), the compositions of tourmalines from INT#1 crosses the schorl–dravite line. Those below this line may imply enrichment in Fe^{3+}. In the case of tourmaline I, this conclusion is supported by the similar position of tourmaline I from the TBZ. In the case of two tourmaline II compositions and one tourmaline III composition charge balance constraints require Fe^{3+}.

Thus, tourmalines I, II, and III from INT#1 differ in isomorphic substitutions from each other. The average chemical composition of the zoned crystals is similar to tourmaline III. Therefore, the simultaneous crystallization of these two tourmalines is likely. The tourmaline I, II, and III compositions are comparable with the compositions of tourmalines I, II, and III from the TBZ (Tables 1 and 3).

5.3. Intrusions #2 and #3 (INT#2 and INT#3)

In these intrusions, two morphological varieties of tourmaline were identified that are similar to those in the TBZ and INT#1. These are zoned aggregates of fine crystals (Figure 4g–i) with rosettes (Figure 4j–k) and euhedral crystals that are up to a few ten's micrometers across (Figure 4l). However, in these intrusions (INT#2 and INT#3), the rosettes were light green to colorless probably due to the lower Fe concentration. We have only determined the tourmaline composition from those in INT#3.

On the BSE image (Figure 4k). two tourmaline generations can be distinguished. Tourmaline II has a nearly black core and a grey rim, whereas tourmaline I has a homogenous color with no zonation.

On the triangular plot X-vacancy–Ca–Na(+K), the tourmaline compositions of both generations plot in the alkali and X-vacant fields (Figure 5e).

Calculations indicate that the Y site in both tourmaline generations was dominated by Mg (Table 4). On the binary plot, excess charge versus Fe_{tot} + Mg + X-vacancy (Figure 5f), most compositions are between X-vacancy–Mg–O root name ("oxy-magnesio-foitite"), dravite, and uvite points, or between two exchange vectors $AlO(R(OH))_{-1}$ and $CaR(NaAl)_{-1}$, where R = Mg, Fe^{2+}. The tourmaline I compositions are above the schorl–dravite line, whereas the tourmaline II compositions are both above and slightly below this line. Such a position indicates an insignificant proportion of Fe^{3+} in the tourmaline compositions. This is supported by the charge balance, which does not require Fe^{3+} except for some of the tourmaline II compositions. In this diagram, the compositions of both tourmaline generations are arranged like those of tourmalines III and IV from the TBZ (Figure 5b). The average chemical composition of tourmaline I (Table 4) is comparable to tourmaline III from the TBZ and intrusion #1 (Table 1). Therefore, we can assume that tourmaline I from INT#3 and tourmaline III in the TBZ and INT#1 were simultaneous.

On the binary plot X-site vacancy versus Ca, the compositions of tourmaline I and II are not clearly parallel to any exchange vector (Figure 6e). This indicates the involvement of all the exchange vectors. Due to a limited number of tourmalines analyzed (Table 4), we did not calculate correlation coefficients for tourmaline I. The highest correlation coefficients for the tourmaline II compositions were calculated between the Na + Mg and X-vacancy + Al_{tot} (−0.82) and Ca + $^{W}O^{2-}$ and Na + $^{W}OH^{-}$ (−0.87). These values indicate that the preferred substitutions in tourmaline II are Na + Mg → X-vacancy + Al_{tot} and Ca + $^{W}O^{2-}$ → Na + $^{W}OH^{-}$. The former substitution was also established for tourmaline IV from the TBZ.

Structural formula calculations show that the euhedral tourmaline crystals can be classified as dravite and schorl (Table 4). In Figures 5e and 6e, the compositions are similar to those of tourmaline II from the TBZ and INT#1. On the triangular plot $Fe_{60}Al_{40}$–Al_{tot}–$Mg_{60}Al_{40}$ (Figure 6f), the compositions of tourmalines from INT#3 plot above and below the schorl–dravite line. The location of two euhedral crystals below this join may imply enrichment in Fe^{3+}. This is indirectly supported by the charge balance constraints that require some Fe^{3+}. Thus, the euhedral tourmaline crystals from INT#3 could be simultaneous with tourmaline II from the TBZ and INT#1. Tourmaline I from the zoned aggregate could have formed simultaneously with tourmaline III from the TBZ and INT#1 and prior to the fine-acicular aggregates, whereas tourmaline II is possibly simultaneous with tourmaline IV from the TBZ. The Cl content in the tourmaline II from INT#3 is 0.25 wt % which is close to that of tourmaline IV and additionally supports their simultaneous crystallization.

Summarizing all data, we can conclude that tourmalines at the Kışladağ deposit are represented by two morphological varieties, aggregates of fine crystals (rosettes, fan-shaped) and larger isolated crystals and their aggregates. Four tourmaline generations are different in their composition and substitutions. Tourmaline I in TBZ and INT#1 is distinguished by the highest Fe_{tot} and enriched in Fe^{3+}. Whereas tourmalines II and III in the same host-rocks present as fine aggregates and characterized by lower Fe_{tot} and Fe^{3+} are accompanied by the formation of isolated crystals and their aggregates. Tourmaline IV is characterized by the lowest Fe_{tot} and is enriched in Cl. It has the highest proportion of X-site vacancy of all the tourmalines.

Table 4. Chemical composition of tourmaline from INT#3.

Component, wt %	Fine-Acicular Aggregates		Crystal
	Tur I (*n* = 5)	**Tur II (*n* = 17)**	**(*n* = 3)**
B_2O_3	10.88 (0.12)	10.81 (0.21)	10.71 (0.23)
SiO_2	36.63 (0.91)	35.56 (1.95)	36.72 (0.96)
TiO_2	0.87 (0.44)	0.15 (0.17)	0.82 (0.21)
Cr_2O_3	*bdl*	*bdl*	*bdl*
V_2O_3	0.07 (0.07)	*bdl*	0.11 (0.02)
Al_2O_3	33.73 (2.74)	36.30 (1.97)	30.13 (3.12)
FeO_{tot}	4.91 (1.03)	2.38 (1.51)	8.88 (4.64)
MnO	*bdl*	0.07 (0.06)	*bdl*
MgO	8.52 (1.24)	8.58 (0.79)	8.09 (1.01)
CaO	1.81 (0.20)	0.93 (0.35)	1.80 (0.47)
K_2O	*bdl*	*bdl*	*bdl*
Na_2O	1.36 (0.29)	1.55 (0.36)	1.63 (0.19)
F	*n.a.*	*n.a.*	*n.a.*
Cl	*bdl*	0.05 (0.06)	*bdl*
H_2O	3.46 (0.07)	3.57 (0.15)	3.66 (0.13)
2F=O			
2Cl=O			
Total	102.23 (1.25)	99.95 (2.35)	102.54 (0.51)
Si	5.851	5.717	5.960
^{T}Al	0.149	0.283	0.040
Total T	6.000	6.000	6.000
^{Z}Al	6.000	6.000	5.723
^{Z}Mg			0.277
Total Z	6.000	6.000	6.000
Fe^{3+}			
Fe^{2+}	0.656	0.321	1.206
^{Y}Al	0.201	0.594	
^{Y}Mg	2.030	2.057	1.680
Ti	0.104	0.018	0.100
Mn		0.010	
V	0.009		0.014
Cr			
Total Y	3.000	3.000	3.000
Na	0.422	0.484	0.511
Ca	0.310	0.161	0.313
X-vacancy	0.268	0.355	0.174
K			
Total X	1.000	1.000	1.000
$^{V}OH^{-}$	3.000	3.000	3.000
$^{W}O^{2-}$	0.311	0.153	0.035
WOH^{-}	0.689	0.834	0.965
Cl		0.013	
F			
Total W	1.000	1.000	1.000
Al_{tot}	6.351	6.878	5.763
Fe_{tot}	0.656	0.320	1.206
Mg_{tot}	2.030	2.057	1.957

6. Discussions and Conclusions

Tourmaline is common in many mineralized systems, such as copper, silver-gold, tin -tungsten, massive sulfide, and uranium deposits, where it makes up breccia cement and clasts, veins, and alterations [6,23–26]. The mineralogical and chemical variations in tourmalines can be especially significant in magmatic and hydrothermal systems where the composition reflects the variability in mineralizing conditions. In addition, it is possible to determine if its constituents are from the primary magmatic-hydrothermal systems: [24,27,28] or from external fluids: [26,29,30]. Tourmaline is useful in prospecting and exploration for porphyry-style deposits (Cu, Au, Sn) [6]. In such deposits, tourmaline often exhibits characteristic features, such as the presence in several generations, Fe → Al substitution, and an evolution from Fe-rich to Mg-rich varieties resulting from late-stage sulfide deposition. In addition, the total Mg and maximum Fe (a.p.f.u.) contents of tourmalines are distinguishing features for different porphyry Cu and Au deposits [6].

The compositions of tourmaline from the Kışladağ gold deposit have a strong similarity to tourmalines from porphyry copper and gold deposits [6–10]. At the Kışladağ deposit, it is present in the tourmaline-bearing breccia zone (TBZ) and intrusive rocks that have undergone potassic, phyllic (tourmaline-white mica-pyrite), and advanced argillic alteration. Four tourmaline generations with different compositions and substitutions have been identified. In general, the tourmaline evolves from calcic and alkali Fe-rich species with a high Fe^{3+}/Fe_{tot} ratio, to species that are depleted in Fe X-vacancy with low a Fe^{3+}/Fe_{tot} value. The interesting feature of the late tourmaline is its relatively high Cl content.

Early Fe-rich tourmaline, with a high Fe^{3+}/Fe_{tot} ratio, was also identified in the propylitic alteration of the gold deposits of the Darasun gold district [6,31], and porphyry copper deposits at Vetka in northeast Russia and Kafan, Armenia [31,32]. In addition, the composition of matrix tourmaline from the Donoso copper-rich breccia pipe in Chile [10] gives a similar high Fe^{3+}/Fe_{tot} ratio of 0.4–0.5. It should be noted that the real Fe^{3+}/Fe_{tot} ratio is higher than that calculated. Considering these observations, we conclude that the tourmaline I at the Kısladağ deposit can be attributed to the potassic stage in INT#1 and early tourmaline in the TBZ. It is likely that these were formed simultaneously at similar f_{O2}. Oyman and Dyar [8] studied tourmaline only from the breccia zone; therefore, the compositions published in their paper correspond to tourmaline I.

Tourmalines II and III from the TBZ and INT#1 are characterized by substantially lower Fe_{tot} and Fe^{3+}/Fe_{tot} ratio and are probably related to the phyllic alteration stage. The lower Fe content in tourmaline is caused by the simultaneous formation of sulfide minerals. This same pattern was observed at the Peschanka porphyry Cu-Mo-Au and Darsun Au deposits [6] and the Michurino epithermal Ag–Au–Cu–Pb–Zn prospect [33]. The correlation coefficient between Al + $^{W}O^{2-}$ and Fe_{tot} + $^{W}OH^{-}$ for tourmalines II and III from the TBZ and INT#1 are −0.65 and −0.82, respectively. This implies a coupled substitution of Al + $^{W}O^{2-}$ ↔ Fe_{tot} + $^{W}OH^{-}$, which is common for tourmaline from quartz-sericite (phyllic) alteration in porphyry copper and gold deposits [6,33].

Among the hydrothermal tourmalines, those formed in argillic zones have a high X-vacancy proportion [34,35]. It is noteworthy that X-vacant tourmaline associated with sulfide minerals in argillic zones have a low Fe content. This was observed at the Vesenny porphyry copper prospect in Chukotka [36], at the margins of the Berezovskoe gold deposit in the Urals [37], and the Kochbulak epithermal gold-telluride deposit in Uzbekistan (Baksheev, unpub. data). In the absence of sulfide minerals, tourmaline from argillic alteration zones can be both Fe-depleted and Fe-rich [34,35]. Tourmaline IV from the TBZ and tourmaline II from INT#3 are distinguished by the proportion of high X-site vacancy. Considering the literature data, such tourmalines can be attributed to the argillic stage of the hydrothermal process and are highly depleted in Ca [35]. However, argillic tourmaline from the Kışladağ deposit is enriched in Ca. A similar calcium-rich X-vacant-Mg-O tourmaline was described from the Biely Vrch porphyry gold deposit in Central Slovakia, but in this case, tourmaline was attributed to the early potassic alteration [38]. At these deposits, tourmaline in the argillic alteration is also associated with Ca carbonate (dolomite, calcite) indicating elevated f_{CO2}, which results in the

partitioning of Ca into carbonate, rather than into tourmaline. At Kışladağ, no carbonate associated with argillic tourmaline was observed. Therefore, we propose that the argillic altered rocks were formed at low f_{CO2} and Ca was incorporated into tourmaline. It should be noted that no other Ca minerals were identified in association with tourmaline from the argillic alteration.

Another interesting feature of the Kışladağ argillic tourmaline IV is the enrichment in Cl. Chlorine-bearing tourmaline was described from the early potassic alteration at the Biely Vrch porphyry gold deposit [38], and the cement of aeolian sandstone in southwestern Poland [39]. The Biely Vrch tourmaline crystallized from an unusual Cl-rich high-temperature fluid [38], whereas tourmaline from the sandstone cement in Poland was related to the low-temperature diagenesis of evaporite sediments inducing reactions of quartz and clay minerals [39]. The fluid inclusion study at the Kışladağ deposit [13] revealed a high-temperature, highly saline fluid was responsible for the formation of most of the gold-bearing veins. It can be ruled out that this fluid was released from fluid inclusions during the late epithermal overprint and incorporated into the Cl-rich tourmaline. However, we have no definitive information for the source of the Cl at present.

In conclusion, the chemical data of tourmalines from the Kışladağ gold deposit has helped in understanding its formation during various alteration/mineralizing (potassic/propylitic), phyllic and argillic stages in a telescoped porphyry/epithermal system. The data is consistent with the fluid inclusion data for Kışladağ deposit [13] that supported the process of an epithermal overprint of the porphyry mineralization.

Author Contributions: Investigation, Ö.B., N.H., and G.B., formal analysis, I.A.B. and V.Y.P., writing—original draft preparation, Ö.B., I.A.B., N.H., G.B., and D.A.B., resources, Ö.B., N.H., G.B., D.A.B., I.A.B., Y.Ö., and V.Y.P. All authors have read and agreed to the published version of the manuscript.

Funding: V.Y. Prokofiev is grateful for financial support from the Russian Science Foundation, Project No. 20–17–00184.

Acknowledgments: The authors would like to thank the TÜPRAG mining company for their permission to investigate the mining site.

Conflicts of Interest: The authors declare no conflict of interest.

References

1. Dyar, M.D.; Taylor, M.E.; Lutz, T.M.; Francis, C.A.; Guidotti, C.V.; Wise, M. Inclusive chemical characterization of tourmaline: Mössbauer study of Fe valence and site occupancy. *Am. Miner.* **1998**, *83*, 848–864. [CrossRef]
2. Hawthorne, F.C.; Henry, D.J. Classification of the minerals of the tourmaline group. *Eur. J. Miner.* **1999**, *11*, 201–215. [CrossRef]
3. Henry, D.J.; Novák, M.; Hawthorne, F.C.; Ertl, A.; Dutrow, B.L.; Uher, P.; Pezzotta, F. Nomenclature of the tourmaline supergroup minerals. *Am. Miner.* **2011**, *96*, 895–913. [CrossRef]
4. Henry, D.J.; Guidotti, C.V. Tourmaline as a petrogenetic indicator mineral—An example from the staurolite grade metapelites of NW Maine. *Am. Miner.* **1985**, *70*, 1–15.
5. Koval, P.V.; Zorina, L.D.; Kitajev, N.A.; Sipiridonov, A.M.; Ariunbileg, S. The use of tourmaline in geochemical prospecting for gold and copper mineralizaIion. *J. Geochem. Explor.* **1991**, *40*, 349–360. [CrossRef]
6. Baksheev, I.; Prokofiev, V.Y.; Zaraisky, G.; Chitalin, A.; Yapaskurt, V.; Nikolaev, Y.; Tikhomirov, P.; Nagornaya, E.; Rogacheva, L.; Gorelikova, N.; et al. Tourmaline as a prospecting guide for the porphyry-style deposits. *Eur. J. Miner.* **2012**, *24*, 957–979. [CrossRef]
7. Yavuz, F.; Iskenderoglu, A.; Jiang, S.Y. Tourmaline compositions from the Salikvan porphyry Cu-Mo deposit and vicinity. *Can. Miner.* **1999**, *37*, 1007–1024.
8. Oyman, T.; Dyar, M.D. Chemical substitutions in oxidized tourmaline in granite-related mineralized hydrothermal systems, Western Turkey. *Can. Miner.* **2007**, *45*, 1397–1413. [CrossRef]
9. Lynch, G.; Ortega, J. Hydrothermal alteration and tourmaline–albite equilibria at the Coxheath porphyry Cu–Mo–Au deposit, Nova Scotia. *Can. Miner.* **1997**, *35*, 79–94.

10. Skewes, M.A.; Holmgren, C.; Stern, C.R. The Donoso copper-rich, tourmaline-bearing breccias pipe in central Chile: Petrologic, fluid inclusion and stable isotope evidence for an origin from magmatic fluid. *Miner. Depos.* **2003**, *38*, 2–21. [CrossRef]
11. Bozkaya, G.; Hanilçi, N.; Baksheev, V.Y.; Banks, D.A. Tourmaline composition of the Kışladağ Au deposit, Uşak, Turkey. Meeting Abstract. *Acta Geol. Sin. Engl.* **2014**, *88*, 520–521. [CrossRef]
12. Baker, T.; Bickford, D.; Juras, S.; Lewis, P.; Oztas, Y.; Ross, K.; Tukac, A.; Rabayrol, F.; Miskovic, A.; Friedman, R.; et al. The Geology of the Kışladağ Porphyry Gold Deposit, Turkey. In *Tectonics and Metallogeny of the Tethyan Orogenic Belt*; Richards, J.P.R., Ed.; Special Publication Society of Economic Geologists, GeoScienceWorld: Virginia, VA, USA, 2016; Volume 19, pp. 57–83.
13. Hanilçi, N.; Bozkaya, G.; Banks, D.A.; Bozkaya, Ö.; Prokofiev, V.; Öztaş, Y. Fluid Inclusion Characteristics of the Kışladağ Porphyry Au Deposit, Western Turkey. *Minerals* **2020**, *10*, 64. [CrossRef]
14. Karaoğlu, Ö.; Helvacı, C. Growth, destruction and volcanic facies architecture of three volcanic centres in the Miocene Uşak–Güre basins: A contribution to the discussion on the development of east–west and north trending basins in western Turkey. *Geol. Mag.* **2012**, *134*, 163–175.
15. Karaoğlu, Ö.; Helvacı, C.; Ersoy, Y. Petrogenesis and $^{40}Ar/^{39}Ar$ geochronology of the volcanic rocks of the Uşak-Güre basin, western Türkiye. *Lithos* **2010**, *119*, 193–210. [CrossRef]
16. Juras, S.; Miller, R.; Skayman, P. Technical Report for the Kışladağ Gold Mine. *Prep. Eldorado Gold* **2010**, *150*, 43–101.
17. Bozkaya, Ö.; Bozkaya, G.; Hanilçi, N.; Laçin, D.; Banks, D.A.; Uysal, I.T. Mineralogical and geochemical evidence of late epithermal alteration in the Kisladag porphyry gold deposit, Usak, Western Turkey. In *Life with Ore Deposits on Earth, Proceedings of the 15th Biennial SGA Conference, Glasgow, UK, 27–30 August 2019*; Society for Geology Applied to Mineral Deposits, University of Glasgow: Scotland, UK, 2019; Volume 3, pp. 1031–1034.
18. Lowell, J.D.; Guilbert, J.M. Lateral and vertical alteration-mineralization zoning in porphyry ore deposits. *Econ. Geol.* **1970**, *65*, 373–408. [CrossRef]
19. Sillitoe, R.H. The tops and bottoms of porphyry copper deposits. *Econ. Geol.* **1973**, *68*, 799–815. [CrossRef]
20. Jarozewich, E. Smitsonian microbeam standards. *J. Res. Natl. Inst. Stand. Technol.* **2002**, *107*, 681–685. [CrossRef]
21. Dutrow, B.L.; Henry, D.J. Complexly zoned fibrous tourmaline, Cruzeiro mine, Minas Gerais, Brazil: A record of evolving magmatic and hydrothermal fluids. *Can. Miner.* **2000**, *38*, 131–143. [CrossRef]
22. Henry, D.J.; Dutrow, B.L. Ca substitution in Li-poor aluminous tourmaline. *Can. Miner.* **1990**, *28*, 111–124.
23. Slack, J.F.; Herriman, N.; Barnes, R.G.; Plimer, I.R. Stratiform tourmalinites in metamorphic terranes and their geologic significance. *Geology* **1984**, *12*, 713–716. [CrossRef]
24. Pirajno, F.; Smithies, R.H. The FeO/FeO + MgO ratio of tourmaline: A useful indicator of spatial variations in granite-related hydrothermal mineral deposits. *J. Geochem. Expl.* **1992**, *42*, 371–382. [CrossRef]
25. Slack, J.F. Tourmaline associations with hydrothermal ore deposits. *Rev. Miner.* **1996**, *33*, 559–641.
26. Xavier, R.P.; Wiedenbeck, M.; Trumbull, R.B.; Dreher, A.M.; Monteiro, L.V.S.; Rhede, D.; de Araújo, C.E.G.; Torresi, I. Tourmaline B-isotopes fingerprint marine evaporites as the source of high-salinity ore fluids in iron oxide copper-gold deposits, Carajás Mineral Province (Brazil). *Geology* **2008**, *36*, 743–746. [CrossRef]
27. Mlynarczyk, M.S.J.; Williams-Jones, A.E. Zoned tourmaline associated with cassiterite: Implications for fluid evolution and tin mineralization in the San Rafael Sn-Cu deposit, southeastern Peru. *Can. Miner.* **2006**, *44*, 347–365. [CrossRef]
28. Dini, A.; Mazzarini, F.; Musumeci, G.; Rocchi, S. Multiple hydro-fracturing by boron-rich fluids in the Late Miocene contact aureole of eastern Elba Island (Tuscany, Italy). *Terra Nova* **2008**, *20*, 318–326. [CrossRef]
29. Palmer, M.R.; Slack, J.F. Boron isotopic composition of tourmalines from massive sulfide deposits and tourmalinites. *Contrib. Miner. Pet.* **1989**, *103*, 434–451. [CrossRef]
30. Peng, Q.M.; Palmer, M.R. The Paleoproterozoic Mg and Mg-Fe borate deposits of Liaoning and Jilin Provinces, northeast China. *Econ. Geol.* **2002**, *97*, 93–108. [CrossRef]
31. Baksheev, I.A.; Prokofiev, V.Y.; Yapaskurt, V.O.; Vigasina, M.F.; Zorina, L.D.; Soloviev, V.N. Ferric-iron-rich tourmaline from the Darasun gold deposit, Transbaikalia, Russia. *Can. Miner.* **2011**, *49*, 263–276. [CrossRef]
32. Baksheev, I.A.; Chitalin, A.F.; Yapaskurt, V.O.; Vigasina, M.F.; Bryzgalov, I.A.; Ustinov, V.I. Tourmaline in the Vetka porphyry copper-molybdenum deposit of the Chukchi Peninsula of Russia. *Mosc. Univ. Geol. Bull.* **2010**, *65*, 27–38. [CrossRef]

33. Baksheev, I.A.; Plotinskaya, O.Y.; Yapaskurt, V.O.; Vigasina, M.F.; Bryzgalov, I.A.; Groznov, E.O.; Marushchenko, L.I. Tourmaline from deposits of the Birgil'da–Tomino ore cluster, South Urals. *Geol. Ore Depos.* **2012**, *54*, 458–473. [CrossRef]
34. Choo, C.O. Mineralogical studies on complex zoned tourmaline in diaspore nodules from the Milyang clay deposit, Korea. *Geosci. J.* **2003**, *7*, 151–156. [CrossRef]
35. Collins, A.C. Mineralogy and Geochemistry of Tourmaline in Contrasting Hydrothermal Systems: Copiapó Area, Northern Chile. Master's Thesis, Department of Geosciences, University of Arizona, Tucson, AZ, USA, 2010; p. 225.
36. Nagornaya, E.V. Mineralogy and Zoning of Porphyry Copper-Molybdenum Field Nakhodka, Chukotka. Ph.D. Thesis, Geological Faculty, Moscow State University, Moscow, Russia, 2014; p. 171. (In Russian)
37. Kudrayvtseva, O.E.; Baksheev, I.A. Compositional variations in tourmalines from the Berezovskoe gold deposit, Central Urals. *Zap. Ross. Miner. O-va* **2003**, *3*, 108–125. (In Russian)
38. Bačík, P.; Kodéra, P.; Uher, P.; Ozdín, D.; Jánošík, M. Chlorine-enriched tourmalines in hydrothermally altered diorite porphyry from the Biely Vrch porphyry gold deposit (Slovakia). *Can. Miner.* **2015**, *53*, 643–691. [CrossRef]
39. Pieczka, A.; Buniak, A.; Majka, J.; Harryson, H. Si-deficient foitite with Al and B from the 'Ługi-1' borehole, southwestern Poland. *J. Geosci.* **2011**, *56*, 389–398. [CrossRef]